Title
Characterization of the Pore Structure of Porous Media Using non-Newtonian Fluids

Journal
Water Resources Research, 55(8)

ISSN
0043-1397

Authors
Hauswirth, Scott C
Najm, Majdi R Abou
Miller, Cass T

Publication Date
2019-08-01

DOI
10.1029/2019wr025044

Peer reviewed

Characterization of the Pore Structure of Porous Media Using Non-Newtonian Fluids

Scott C. Hauswirth[1], Majdi R. Abou Najm[2], and Cass T. Miller[3]

[1] California State University, Northridge, Department of Geological Sciences, Northridge, California, USA.

[2] University of California, Davis, Department of Land, Air, and Water Resources, Davis, California, USA.

[3] University of North Carolina Chapel Hill, Department of Environmental Sciences and Engineering, Chapel Hill, North Carolina, USA.

Corresponding author: Majdi R. Abou Najm (mabounajm@ucdavis.edu)

Key Points:

- A simple, low-cost method using non-Newtonian fluids to characterize pore structure is presented
- Method validated for three sands and a polydisperse sand bead mixture using experimental results and x-ray pore characterization
- Results indicate good agreement with x-ray pore size distributions, and saturated water flow and drainage curve experimental data

Abstract

We demonstrate a simple, cheap method for pore size characterization of porous media that generates a distribution of pore radii for improved flow and transport modeling. The new method for pore structure characterization utilizes recent theoretical developments in non-Newtonian fluids. Numerical evaluations and validations with synthetic porous media showed potential for obtaining a distribution of effective pore radii and their contribution to total flow only by complementing water with non-Newtonian fluids in saturated infiltration experiments. To demonstrate this ability on real sands, a series of one-dimensional column experiments was conducted with varying porous medium packings, including Accusands and a polydisperse sand/glass bead mixture. For each packing, distilled water and varying concentrations of guar and xanthan gum were injected over a range of flow rates and pressure gradients. The model-generated pore radii were compared with pore radius distributions measured by x-ray micro-computed tomography (µCT), with results demonstrating good agreement between the model and µCT data. Simulations of saturated water flow and drainage curves using model-generated pore radii compared favorably to experimental data, with errors typically between 2-10% for single-phase flow and approaching the error of the µCT measured radius distributions for the drainage curves.

Plain Language Summary

Knowledge of pore sizes of porous materials is critical to modeling water flow in the environment. Most pore size measurement methods are expensive and require collecting samples of a limited size for laboratory analysis, thus possibly disturbing the pore structure. Our method shows promise as a simple, cheap approach to measure pore sizes directly in the field. The method involves flowing food-grade fluids that exhibit specific flow properties (non-Newtonian fluids) through soils and using the results as input for the model that provides a pore size distribution. We tested the method on four sands, conducting flow experiments with water and six different non-Newtonian fluids. Model results showed good agreement with direct x-ray measurements of the sands. We also used the pore sizes produced by the model to calculate the flow of water through the sands and compared these results with experimental data. We obtained excellent agreement, with errors on the order of 2-10% for water flow and approaching the error obtained using the x-ray results for the drainage of the material. These results indicate that this simple method provides results nearly as accurate as much more expensive and invasive methods and shows promise for use in the field.

1 Introduction

Non-Newtonian fluids are important for a wide-range of applications, including hydraulic fracturing, processed food production, industrial processes, enhanced oil recovery, and environmental remediation (Lakhtychkin et al., 2012; Tosco & Sethi, 2010; Sochi, 2010; Hauswirth et al., 2012; Hauswirth & Miller, 2014; Silva et al., 2017; Jang et al., 2015; Stewart et al., 2014). Recently, Abou Najm and Atallah (2016), Atallah and Abou Najm (2019), and Bassett, et al. (2019) presented a new method using non-Newtonian fluids to characterize the pore space of porous medium systems. The goal of this approach is to provide a simple, non-destructive method to determine effective pore sizes of a porous medium, which can in turn be used to improve modeling of fluid flow and pollutant transport through the medium under both saturated and unsaturated conditions. This approach conceptualizes porous media as a capillary bundle model composed of groups of capillary tubes of N representative radii (R_i), with each tube size contributing a discrete fraction (w_i) of the overall flow. The model only requires inputs of N combinations of head and flow rate data from saturated flow experiments conducted with water and N-1 non-Newtonian fluids. The utility of the approach was illustrated experimentally with synthetic porous media (Atallah & Abou Najm, 2018) and numerically with simulations (Abou Najm & Attalah, 2016) of flow through "virtual" porous medium systems of digitized pore size distributions for six soils from the literature. Results showed that four pore radii (N=4), thus data for four fluids, were sufficient to characterize both saturated and unsaturated flow through those soils.

Standard approaches for characterizing flow typically involve the determination of a single permeability or the use of calibrated dual or multi-permeability models (Larsbo, et al., 2005; Vogel et al., 2000; Gerke & van Genuchten, 1993). However, these approaches incorporate limited information regarding the pore structure itself, and therefore may fail when applied to conditions outside calibrated boundaries. Alternatively, knowledge of the pore size structure of a porous medium can be used to directly inform flow and transport properties, including intrinsic and relative permeabilities (Jerauld and Salter, 1990; Burdine, 1953; Al-Raoush, & Willson, 2005; Culligan, et al. 2006; Joekar-Niasar, 2008; Gao & Hu, 2013) and dispersivity (Bijeljic & Blunt 2006; Bijeljic & Blunt 2007), or used to direct model flow (Bultreys et al., 2016). A number of methods have been employed to characterize pore structure, including: direct measurement using micrography (with or without impregnation with resin) (Loucks et al., 2009; Vogel, 1997; Doyen, 1988); gas adsorption (Dollimore & Heal, 1964; Groena et al., 2003); mercury intrusion porosimetry (MIP) (Giesche, 2006; Gao & Hu, 2013; Zhou et al., 2017); x-ray micro-computed tomography (µCT) or MRI imaging (Lindquist et al., 2000; Wildenschild & Sheppard, 2013; Komlosh et al., 2011); small-angle x-ray scattering (Omote & Ito, 2003); and nuclear magnetic resonance (NMR) (Strange et al., 1993; Gallegos & Smith, 1988; Kenyon et al., 1989). A recent method has been reported that uses yield stress fluids (i.e., Bingham, Herschel-Buckley fluids) and a capillary bundle model to determine Gaussian mono- and multimodal pore size distributions based on a series of flow experiments conducted by incrementally increasing the pressure drop across a rock core. This method aims to provide a laboratory-based replacement for MIP due to its use of toxic mercury, and positive results have been demonstrated with sandstone cores (Oukhlef et al., 2014; Rodriquez de Castro et al., 2014, 2016).

These approaches share one or more significant limitations. All methods require that samples be collected and analyzed *ex situ*. While sampling procedures and apparatus exist to minimize disturbance, these may not result in perfectly undisturbed samples, especially for less cohesive materials. Removal of samples also precludes monitoring of changes in the system over time. Sample sizes are small, typically on the order of 1-10 cm^3 for most of the methods. For many of the imaging methods (e.g., µCT), there is additionally a trade-off between resolution and sample size. This trade-off may require choosing between sufficiently resolving matrix pores and capturing larger scale features such as macropores, making characterization of the pore structure of dual-porosity soils in the field at a scale above the REV impossible in most situation. There are additional practical concerns with many of these methods, including the cost of sophisticated equipment such as µCT and MRI, and the hazards associated with the use of mercury in MIP.

Ideally, it would be useful to have a method allowing non-destructive characterization of pore space *in situ*. Methods using liquid latex and shear-thinning fluids have been applied to identify and quantify preferential flow paths in field soils, however these approaches address only the large-scale pores such as mud cracks, insect burrows and similar features (Stewart et al., 2014; Abou Najm et al., 2010). The Abou Najm and Atallah method (hereafter referred to as ANA) raises the possibility of using relatively simple flow experiments to fully characterize porous media non-destructively in the field, capturing both macro- and micropores. Conducted either *in situ* or *ex situ* with undisturbed soil cores, the method requires only safe, inexpensive, and readily available materials. For example, a laboratory implementation could be conducted with a simple constant head permeameter, a balance, water, and xanthan gum.

The goal of this work is to apply the ANA method to real porous medium systems to assess the model's ability to characterize the pore structure, both in terms of producing accurate pore radii and in providing more information than would be available from traditional, single-fluid based approaches. Specific objectives include: (1) characterizing the pore size distributions of four unconsolidated media with µCT and four image analysis methods; (2) determining sands' effective pore radii with the ANA numerical solver using inputs from results of water and non-Newtonian flow experiments; (3) assessing the accuracy of the pore size distributions produced by the ANA model; and (4) evaluating the added utility of obtaining multiple pore size classes over the single effective radius obtained from Newtonian fluid approaches.

2 Materials and Methods

2.1 Experimental

Distilled, deionized water (DDI) was produced using a Dracor water system (Durham, NC, USA). Guar gum was obtained from SNP, Inc. (Durham, NC, USA) and sodium azide and xanthan gum were obtained from Fisher Scientific. Sands (Accusand) and glass beads used for column experiments were obtained from U.S. Silica and Fisher, respectively.

Three solutions each of guar and xanthan gum were produced. Guar gum solutions were produced at nominal concentrations of 0.5, 3, and 5 g/kg, and xanthan gum solutions were produced at 0.5, 1, and 2.5 g/kg. After dissolving the appropriate amount of powdered gum and sodium azide as a biocide (0.1 wt.%), the mixture was vacuum filtered through a 2.5-µm glass fiber filter (Baxter Scientific) to remove undissolved material. Solutions were stored at 4°C and were used within 7d to minimize any potential temporal changes to the solution properties.

Rheological properties of the fluids were measured with a TA Instruments AR-G2 rotational rheometer with a cone-and-plate configuration. The cone was 40mm, with a 1° angle and the plate was equipped with an integrated Peltier temperature control unit. A one-minute pre-shear was performed at a constant shear rate of 1 s^{-1}, after which measurements were collected in torque-controlled mode, with a torque range of approximately 0.05 to 500 µN·m. The apparent viscosity (η; Pa·s) and shear rate ($\dot{\gamma}$; s^{-1}) values were then fit to the Cross model (Cross, 1965):

$$\eta = \eta_\infty + \frac{\eta_0 - \eta_\infty}{1 + k\dot{\gamma}^{1-\alpha}} \quad (1)$$

where η is the apparent viscosity (Pa·s), η_∞ is the infinite-shear viscosity (Pa·s), η_0 is the zero-shear viscosity (Pa·s), and k and α are fit parameters.

Table 1. Properties of media used in this study.

Property	12/20 Accusand	20/30 Accusand	40/50 Accusand	High-variance mixture
Length (m)	0.287	0.2617	0.2502	0.2175
Porosity[1]	0.35	0.33	0.32	0.32
Pore volume[1] (m^3)	4.91x10^{-5}	4.26x10^{-5}	3.98x10^{-5}	3.50x10^{-5}
Mean grain size[2] (r; m)	5.7x10^{-4}	3.8x10^{-4}	1.9x10^{-4}	2.8x10^{-4}
Grain size variance	1.0x10^{-4}	2.5x10^{-5}	1.3x10^{-5}	1.7x10^{-4}
Intrinsic permeability[3] (m^2)	2.24x10^{-10}	1.58x10^{-10}	5.80x10^{-11}	2.15x10^{-10}
Inertial permeability[3] (m)	4.0x10^{-7}	6.2x10^{-7}	5.5x10^{-7}	3.34x10^{-7}

1- Determined from length and bulk density

2- Based on sieve analysis

3- Determined by fitting Darcy-Forchheimer equation to water flow experiments

Column experiments were conducted in 2.5-cm inner diameter glass columns (Ace Glass) with packed lengths ranging from 20-30 cm. Columns were packed with four media: 12/20, 20/30, and 40/50 Accusands, and a high variance sand/glass bead mixture (HV) containing twelve sand fractions sieved from Accusands and U.S. Silica F-series sands (#16-80 mesh) and two sizes of glass beads (2mm and 3mm). The Accusands were dry packed, vibrated, and compressed by hand between the air-tight plungers of the columns. The HV medium was moistened prior to loading and only gently vibrated to prevent layering during the packing process. Water and gum solutions were injected vertically upward, controlling the volumetric flow rate with a programmable syringe pump (Harvard Apparatus PHD 4400). The pressure difference across the column was measured with a pressure transducer (Omega PX800). Measured pressures were corrected to account for flow through the unavoidable short sections of influent and effluent tubing using the Hagen–Poiseuille equation for DI and a semi-analytical solution for guar and xanthan gum solutions (Sochi, 2015). Properties of the media are provided in Table 1.

2.2 µCT Analysis

The pore size distribution of each media was determined by x-ray micro-computed tomography (µCT) analysis. Analyses were conducted by the Shared Materials Instrumentation Facility (SMIF) at Duke University using a Nikon XTH 225 ST high-resolution µCT scanner. A 2.5cm to 3.5cm section of each column was scanned at a resolution of between 11.9 to 18.9µm/pixel. The raw scans were converted to images representing horizontal slices of the column. These images were subsequently cropped to remove the glass column wall, contrast enhanced, and normalized using ImageJ. The images were converted to binary in ImageJ using the Otsu algorithm (Otsu, 1979) to threshold each individual image (Figure 1). To account for varying concepts of pore size distributions in porous media and differing approaches for calculating them (Münch & Holzer, 2008), a total of four algorithms were used to compute pore size distributions from the µCT images for each media, specifically:

Table 2. Cross model parameters for fluids used in this study

Fluid	$\eta_\infty\ (Pa \cdot s)$	$\eta_0\ (Pa \cdot s)$	k	α
DI	9.544×10^{-4}	9.544×10^{-4}	---	---
Guar, 0.5g/kg	1.77×10^{-3}	2.32×10^{-3}	5.56×10^{-3}	0.183
Guar, 3g/kg	3.04×10^{-3}	1.36×10^{-1}	1.21×10^{-1}	0.317
Guar, 5g/kg	3.31×10^{-3}	1.36×10^{0}	4.48×10^{-1}	0.293
Xanthan, 0.5g/kg	1.43×10^{-3}	5.32×10^{-2}	0.853	0.402
Xanthan, 1g/kg	1.58×10^{-3}	2.36×10^{-1}	1.63	0.341
Xanthan, 2.5g/kg	2.38×10^{-3}	6.79×10^{0}	13.4	0.234

1. The “continuous pore size distribution” (PSD) tool of the xlib plug-in for ImageJ, which fits spheres of maximum radii within the pore space to produce a pore sizes distribution (Münch & Holzer, 2008);
2. The “mercury intrusion porosimetry” (MIP) simulation of the xlib plug-in, which intrudes spheres of varying radii into the three-dimensional µCT image stack to produce binned counts of pore radii (Münch & Holzer, 2008);
3. The “thickness” function of the BoneJ plug-in for ImageJ (BJT), which calculates the Euclidean distance at each location in the pore space, then generates thickness maps which are converted to volumetric pore size distribution using an image stack histogram (Doube et al., 2010);
4. The “pore size distribution function” of Porespy (PSF), a Python script that also calculates 3D Euclidean distances between grains (Gostick, 2017).

The last two algorithms are similar to the PSD method in that they measure the radius distribution of the entire pore space, regardless of whether that space would be considered a pore throat or a pore body and were used primarily to confirm the PSD analysis.

2.3 Modeling

The theoretical aspects of the ANA modeling approach have been presented previously (Abou Najm & Attallah, 2016). Briefly, the method uses a parallel capillary tube model composed of tubes of N different radii. Each tube size class contributes a fraction (w_i) of the overall flow. Head and flow rate data from flow experiments using water and N-1 non-Newtonian fluids, along with sand characteristics (porosity, tube length, total volume)

and fluid characteristics (rheological parameters) are supplied as inputs. Given these inputs, the numerical model can then be used to solve three problem types:

Type 1: Determination of weights (w_1, w_2,…w_N) of each radius (R_1, R_2,…R_N), given the radii as inputs.

Type 2: Determination of the radii of the tubes, given the weights.

Type 3: Estimation of both weights and radii for the system, given initial guesses and constraints on the solution.

Problem Types 1 and 2 have unique solutions that are obtained by standard numerical solvers in Matlab for linear (Type 1) and non-linear (Type 2) systems of equations. Problem Type 3 has more unknowns (2N) than equations (N), and therefore does not have a unique solution. However, by constraining the maximum ratio between the largest and smallest radii (d_{range}) and the ratio between adjacent radii (d_{adj}), an optimization scheme incorporating a constrained non-linear minimization technique called sequential quadratic programming (SQP) was used by means of the Matlab *fmicon* function to approximate a distinct set of radii-weight solutions.

For this study, the ANA solver was modified to incorporate a semi-analytical solution for tube flow of Cross model fluids (Sochi, 2015; Attallah, 2015) to reduce overall computational work. For all runs, the input data were chosen to minimize pressure measurement errors at very low pressures ($\Delta H/L < 0.1$) and potential non-laminar flow effects at high flow rates ($Re > 1$). The model also requires that the effective length of the capillary tubes be provided; for this work we assumed the Blake-Kozeny-Carman tortuosity of 25/12, rounded to an even value of 2 (Sochi, 2010; Bird et al., 2006); future work will further investigate the role of tortuosity in the model.

3 Results and Discussion

3.1 Experimental and μCT Results

The Cross model parameters for each fluid are provided in Table 2. Pressure-flow rate curves from the column flow experiments are shown in Figure S1 in the Supporting Information. The curves are concave downward, consistent with shear thinning fluids for which viscosity decreases with increasing shear rate. A slight upward concavity is apparent at high flow rates for low concentration solutions, which is presumed to be the result of non-laminar flow behavior. To avoid conflation of effects, a conservative Reynolds number (Re) value of 1 was used as the upper bound for experimental data used as model inputs, where Re was defined by

$$Re = \frac{\rho v \overline{r_p}}{\mu}$$

where ρ is the density (1000 kg/m^3), v is the mean fluid velocity, $\overline{r_p}$ is the mean grain radius, and μ is the dynamic viscosity (η_∞ was used for non-Newtonian fluids since non-Darcy flow occurs at higher flow rates and therefore higher shear rates).

Pore size distributions of the media were determined from the μCT images using the four image analysis algorithms explained earlier (Figure 2). Results are presented as a normalized volume fraction to allow direct visual comparison:

$$\overline{F_V} = \frac{F_{V,i}}{\max(F_{V,i})}, \quad (2)$$

where $\overline{F_V}$ is the normalized volume fraction, and $F_{V,i}$ is the volume fraction of the ith radius.

Normal and log-normal distributions were fit to the pore radii; the Accusands were found to better fit normal distributions, while the HV radii were slightly better fit by a log-normal distribution. Fit parameters are provided in Table S1 in the Supporting Information. As expected, the PSD, BJT, and PSF methods produced similar profiles with the primary difference being slightly broadening distributions in the order: PSF < BJT < PSD. The MIP method consistently resulted in narrower distributions with smaller means than the other methods, a result of the method measuring the pore throat distribution, rather than the total pore radius distribution (Holzer et al., 2016). The pore size distributions of the media were generally as expected: the 40/50 Accusand displayed a distinctly smaller and narrower pore size distribution than the other media; the 12/20 Accusand displayed the largest and broadest pore size distribution; and the 20/30 Accusand and HV fell in the middle. The 20/30 Accusand and HV exhibited a remarkably similar range of pore radii sizes, despite the large difference in the variance of grain size distribution. This similarity was not expected; however, it is consistent with the results of the experimental and model results as described below.

3.2 Modeling Results

The ANA modeling solver was used to calculate pore radii and/or weights for each medium, using Problem Types 1, 2, and 3 as described above. A summary of the model runs conducted for this work is provided in the Supporting Information (Table S2). To compare model radii directly to µCT results, the output from each model run was converted to a volume fraction ($F_{V,i}$) in two ways. First, since the model is based on capillary tubes (i.e., cylindrical pores), the volume fraction was calculated as:

$$F_{V,i} = \frac{(\pi R_i^2) X_i L}{V_p}. \tag{3}$$

Second, because the µCT image processing algorithms are primarily based on inscribed sphere approaches, we also calculated volume fractions based on a spherical pore geometry:

$$F_{V,i} = \frac{\left(\frac{4}{3}\pi R_i^3\right) X_i}{V_p}. \tag{4}$$

For both equations, X_i is the number of radii for the ith radius output by the model, L is the capillary tube length, and V_p is the total pore volume of the medium.

Results of model runs using Type 3 with N=4 are compared to radius distributions from MIP and PSF radius distributions in Figure 3 to illustrate typical modeling results. For each medium, twelve different sets of experimental data (i.e., fluid-flow rate combinations) were used as inputs. Volume fractions were determined for each set of runs assuming both cylindrical and spherical pore geometries. Many runs resulted in fewer than N significant radii, which occurred as one or more pore size classes being assigned very low weights ($w < 1 \times 10^{-10}$) and quantities of pores ($X_i \ll 1$), or, in the case of Problem Type 2, multiple weight classes being assigned identical radii. For the Type 3, N=4 case, many runs produced only one or two significant radii, as evidenced by the large number of radii with $F_{V,i} \approx 1$, which is especially apparent for the 40/50 Accusand and HV media. The dominant radii cluster very near the peak of the MIP distribution for all media except the 12/20 Accusand. The close correspondence of the model results to the MIP distribution, rather than the PSF (and other µCT methods), can be explained by how the model and µCT methods conceptualize the pore space. The ANA model simplifies the pore structure as a network composed solely of tubes, so the returned radii necessarily represent effective radii of interconnected pore body-pore throat systems.

Table 3. Normalized root mean square error (NRMSE) values for saturated water flow simulated using a capillary bundle approach informed by the pore size distributions from the ANA model and compared to the experimental data. NR=no runs conducted.

	40/50			20/30			12/20			HV		
	Type 1	Type 2	Type 3	Type 1	Type 2	Type 3	Type 1	Type 2	Type 3	Type 1	Type 2	Type 3
N=2	NR	0.05	0.05	NR	0.05	0.05	NR	0.13	0.10	NR	0.08	0.06
N=4	0.03	0.03	0.03	0.05	0.07	0.08	0.12	0.11	0.11	0.27	0.05	0.05
N=7	0.03	0.03	0.03	0.08	0.08	0.08	0.12	0.13	0.12	0.05	0.05	0.05
N=10	0.03	0.08	0.03	0.08	0.08	0.05	0.12	0.10	0.11	0.11	0.11	0.10
N=19	0.03	0.09	0.02	0.08	0.09	0.08	0.12	0.12	0.12	0.11	0.11	0.11

Because these radii are determined from pressure-flow relationships, they will tend to reflect a strong influence of pore throats, and would therefore be expected to show better agreement with the MIP distribution, which is effectively a pore throat size distribution (Münch & Holzer, 2008; Holzer et al., 2016; Xiong et al., 2016; Doyen, 1988; Wise, 1992; Srisutthiyahorn & Mavko, 2017). The PSD, BJT, and PSF image analysis methods, conversely, measure the distributions of the radii of spheres fit throughout the entirety of the pore space, without distinguishing between pore throats and pore body, and such a distribution alone would not be expected to directly correlate with the hydraulically determined, effective radii from the model (Münch & Holzer, 2008; Holzer et al., 2016). The effect of calculating $F_{V,i}$ as tubes (Eq. 3) versus spheres (Eq. 4) varied between media. Media that tended to have model results with fewer significant radii (e.g., 40/50 Accusand and HV media), showed little difference between the two geometries. The greatest difference was observed for the 12/20 Accusand, for which the volume fractions of the smallest radii, which were also least correlated to the µCT distributions, were significantly reduced, while the volume fractions of pore sizes in better agreement with the µCT results were increased.

The differences between spherical and cylindrical pores were also apparent when comparing volume-weighted mean pore radii among all problem types. The volume-weighted means ($\overline{R_v}$) were calculated for all model runs using the equation:

$$\overline{R_V} = \sum_{i=1}^{N} R_i F_{V,i} \quad (5)$$

and compared with the corresponding MIP and PSF means obtained from µCT analysis, which represented the extremes of the image processing algorithms used (Figure 2). As shown in Figure 4, for a given medium, the mean pore radii were generally very similar between runs and across problem types, suggesting that the model produces consistent radii regardless of the specific inputs and parameters used. When volume fractions were calculated assuming cylindrical pores (Eq. 3), mean pore radii fell near or below the mean MIP radii, with the greatest deviation observed for the 12/20 Accusand. Calculating the volume fractions as spherical pores (Eq. 4) improved the correlation between the model and µCT data, with the mean of the model results falling between the MIP and PSF means for all media. Notably, the resulting upward shift differs between media, resulting in an increase of roughly 5×10^{-5} m for the 12/20 Accusand, into the range of the µCT data, without increasing significantly for the 40/50 Accusand (which would move the means out of the range of the µCT data). While the fact that the ANA model is based on cylindrical pores would suggest that the spherical assumption would be inappropriate, it may be that a common pore geometry is necessary to allow direct comparison between the µCT and model data on a volume fraction basis.

To further validate the model, the ANA pore distributions were used to simulate water flow with a bundle of capillaries approach for direct comparison with experimental flows using the Hagen-Poiseuille equation:

$$Q = \sum_{i=1}^{N} \frac{\pi X_i R_i^4 \Delta P}{8 \mu L} \tag{6}$$

where Q is the flow rate, ΔP is the pressure drop across the column, and μ is the dynamic viscosity of water at 22°C. Normalized root mean square errors, given by

$$\text{NRMSE} = \frac{\sqrt{\sum (Y_{exp} - Y_{mod})^2}}{\max(Y_{exp}) - \min(Y_{exp})}, \tag{7}$$

were calculated and found to range from 2-13% (with one value of 27%), as tabulated in Table 3. This approach avoids differences in the conceptualization of pore geometry between µCT and the model, as it relies only on the number of pores. The results are consistent with the mean pore size comparison, with error increasing in the order: 40/50 < 20/30, HV < 12/20. The low error overall demonstrates that the model produces pore size distributions that are hydraulically equivalent to the experimental system for single-phase systems.

To evaluate the effect of errors in rheological measurements, a sensitivity analysis was conducted, varying each of the four Cross model parameters for a data set from the 20/30 Accusand experiments (N=4). The results, shown in Figure 5, indicated that all four parameters linearly impact the volume-weighted mean pore radius, with the value of α having the strongest effect $\left(\frac{\delta \overline{R_v}}{\delta \alpha} = 1.3\right)$. Variation of k and η_∞ showed a similar magnitude of effect on $\overline{R_v}$ $\left(\frac{\delta \overline{R_v}}{\delta x} = \sim 0.7\right)$, but in opposite directions. The model was least sensitive to η_∞ $\left(\frac{\delta \overline{R_v}}{\delta \eta_\infty} = \sim 0.3\right)$, likely because the high shear rates at which the infinite shear viscosity arises only occur immediately adjacent to the solid surface at the flow rates used in the experiments.

3.3 Soil Water Characteristic Curve

In addition to assessing the accuracy of the pore radii generated by the model, another objective of this work was to assess the utility of the ANA model as compared to single-fluid approaches. A major advantage of this method is that it results in multiple radii, which is especially important in multiphase systems that cannot be accurately predicted based on a single pore radius. Although most model runs in this study produced fewer than N significant radii, many runs did result in more than one radii. For example, using carefully selected distributions of weights, Type 2 runs frequently produced just under N distinct radii, including up to 17 significant radii for N=19. We used a series of Type 2 runs with N=2-19 to assess the additional value of obtaining multiple radii by estimating water retention curves for the Accusands and comparing with literature values. The capillary pressure head for each radius class was calculated with the Young-Laplace equation (Bear 2013):

$$\Psi_i = \frac{2\sigma \cos\theta}{\rho g R_i} \tag{8}$$

where Ψ_i is capillary pressure head of the ith radius (m), σ is interfacial tension (0.07191 J/m2 for air-water interfacial tension), θ is the contact angle (assumed to be zero), ρ is density (1,000 kg/m3), g is gravitational acceleration, and rR_i is the ith radius.

Simulated primary drainage curves calculated from Type 2 model results for 20/30 Accusand are compared to experimental data extracted from Schroth (1996) in Figure 6a. Qualitatively, for N=1 (i.e., using water only), the single radius resulted in a capillary pressure slightly above the main drainage curve from Schroth (1996), failing to capture either the wet or dry side of the curve. Increasing the number of fluids to N=2 (using the ANA model), results in a slightly better capture of the dry-side of the curve. For all N>2, the wet-side of the curve is well characterized by the simulated results. The results for N=4 to N=10 capture the general trend of the dry side, however, there is some deviation due to overestimation of small-pore volume. The N=19 case correlates remarkably well with both the high and low saturation sides of the curve and is shifted only slightly above experimental data through the mid-saturation values. The NRMSE (Figure 6b) decreases monotonically with increasing N, with a large decrease between N=2 and N=4, and an error for N=19 nearly 70% lower than for N=1. The water retention curve was also simulated using the MIP pore size distribution, and the error for this simulation is only slightly below that of the N=19 model. These results suggest that substantial improvements over single-fluid approaches may be obtained with only water and three additional non-Newtonian fluids or flow rates (i.e., N=4) and with an increasing number of experiments the model can approach the utility of sophisticated imaging methods. It should be noted that no fitting was involved in obtaining the simulated drainage curves; these are predicted directly from the radius distributions produced by the ANA model using data from saturated flow experiments.

The fact that the model resulted in fewer than N distinct radii in many cases is a potential limitation, and the reason for this result is currently being investigated. Since all fluid/flow rates were determined to be independent based on the criteria discussed in Attallah (2015), one possibility is that the distributions of pore sizes in these homogeneous, well-sorted sands are narrow to a degree that the precision of the method is insufficient to resolve separate pore classes. This explanation is supported by the fact that runs for the 40/50 Accusand, which had the narrowest pore size distribution, consistently returned only one or two radii (regardless of N), while still resulting in low error and a consistently strong correlation to µCT pore size distributions. The runs for the 12/20 Accusand and HV media, which had broader pore size distributions, commonly returned three or more significant radii. Further study is underway to investigate this phenomenon. Even with the homogenous sands used in this study, however, it was possible to obtain distributions of pore sizes using Problem Type 2 by varying the input weight distribution.

5 Conclusions

The work described here served as the first validation of the ANA model for real porous medium systems, with two major goals: (1) assess the accuracy of the ANA model with regards to its ability to predict pore radii consistent with physical porous medium systems, and (2) assess the usefulness of the model in characterizing real soils. With perhaps the exception of the 12/20 Accusand, the model effectively identified the pore throat radii (MIP) of the media. Mean pore radii produced by the model were consistent with those determined from µCT and saturated water flow simulated using model-produced radii closely matched the experimental data. The major trends among the varying media were captured (e.g., 40/50 Accusand has smallest and narrowest pore size distribution, 20/30 Accusand had a larger and broader pore size distribution). While the model failed to provide N distinct radii in all cases, it did produce multiple radii in many runs, especially those conducted using Problem Type 2. The results of runs with up to 17 distinct radius classes were used to estimate drainage curves with the Young-Laplace equation, and were found to agree with published experimental results remarkably well. Importantly, the method is not intended to serve as a replacement for sophisticated imaging techniques or computationally demanding models, but rather to provide a convenient and user-friendly approach to improve soil characterization. While the experimental apparatus used in this work included precision syringe pumps and pressure transducers, the method itself is designed to be amenable to the use of simple, safe, and inexpensive apparatus, allowing implementation nearly anywhere, including potentially in *in situ* field applications. For example, a constant head permeameter with piezometers for measuring the head drop cost on the order of USD$200-300 and can be constructed from readily available hardware for considerably less (see, e.g, Attallah & Abou Najm 2019). While further study is recommended to fully address the applicability of the method to a broader range of systems, assess the effect of the precision of rheological and pressure measurements, and adapt it for *in situ* field applications, the results of this work demonstrate that the model provides pore size distributions consistent with both hydraulic characteristics and µCT measurements of porous medium systems and support its suitability for its intended purpose.

Acknowledgments, Samples, and Data

The authors would like to thank Caroline Tapscott, Pamela Schultz, and Christopher Bowers for their assistance with the laboratory experiments. The work of CTM was supported by Army Research Office grant W911NF-14-1-02877, and National Science Foundation grants 1619767 and 1604314. Supporting information is available online and includes: (1) Figure S1 – results of column flow experiments; (2) Table S1 – normal probability distribution parameters fit to µCT data; (3) Table S2 – summary of model runs.

Symbols and Abbreviations

Acronyms and abbreviations

ANA	Abou Najm and Atallah method
BJT	BoneJ (ImageJ) thickness image analysis algorithm
DDI	distilled, deionized water
MIP	Mercury intrusion porosimetry simulation (xlib ImageJ plugin)
NRMSE	normalized root mean square error
PSD	Continuous pore size distribution (xlib ImageJ plugin)
PSF	Porespy pore size distribution function
µCT	Micro-computed x-ray tomography

Greek Letters

α	Cross rheological model exponential parameter
η	Apparent viscosity
η_∞	Infinite shear viscosity (Cross model parameter)
η_0	Zero shear viscosity (Cross model parameter)
$\dot{\gamma}$	Shear rate
μ	Dynamic viscosity
Φ	Capillary pressure head
ρ	Density
σ	Interfacial tension
θ	Contact angle

Symbols

F_V	Volume fraction
$F_{V,i}$	Volume fraction of pore radius class i
$\overline{F_{V,\imath}}$	Normalized volume fraction of pore radius class i
g	Gravitational acceleration
ΔH	Head difference across column
k	Cross model parameter
L	Length of column
N	Number of radius classes
ΔP	Pressure difference across column
Q	Volumetric flow rate
R_i	Radius of pore size class i
$\overline{R_V}$	Volume-weighted mean pore size
Re	Reynolds number
v	Mean flow velocity
V_p	Volume of pore space
w_i	"Weight" = fraction of flow through pores of radius class i
Xi	Number of pores of radius class i

References

Abou Najm, M. R., & Atallah, N. M. (2016), Non-Newtonian fluids in action: revisiting hydraulic conductivity and pore size distribution of porous media. Vadose Zone Journal, 15 (9).

Abou Najm, M. R., Jabro, J. D., Iversen, W. M., Mohtar, R. H., & Evans, R. G. (2010), New method for the characterization of three-dimensional preferential flow paths in the field. Water Resources Research, 46 (2).

Al-Raoush, R.I., & Willson, C.S.(2005), Extraction of physically realistic pore network properties from three-dimensional synchrotron X-ray microtomography images of unconsolidated porous media systems. Journal of Hydrology 300, 44–64.

Atallah, N. M. (2015), Solver for a new theory for revisiting hydraulic conductivity and pore size distribution of porous media. Master's Thesis, American University of Beirut.

Atallah, N. M., & Abou Najm, M. R. (2019), Characterization of synthetic porous media using non-Newtonian fluids: experimental evidence. European Journal of Soil Science, doi.org/10.1111/ejss.12746.

Bassett, C., Abou Najm, M., Ammar, A., Stewart, R., Hauswirth, S., & Saad, G. (2019), Physically based model for extracting dual-permeability parameters using non-Newtonian fluids. Vadose Zone Journal, doi: 10.2136/vzj2018.09.0172.

Bear, Jacob. (2013), Dynamics of Fluids in Porous Media, Courier Corporation.

Bird, R. B., Stewart, W. E., & Lightfoot, E. N. (2006), Transport Phenomena. Revised 2nd ed., John Wiley & Sons, Inc.

Bijeljic, B., & Blunt, M. J. (2006), Pore-scale modeling and continuous time random walk analysis of dispersion in porous media, Water Resources Research, 42, W01202, doi:10.1029/2005WR004578.

Bijeljic, B., & Blunt, M. J. (2007), Pore-scale modeling of transverse dispersion in porous media, Water Resources Research, 43, W12S11, doi:10.1029/2006WR005700.

Bultreys, T., De Boever, W., & Cnudde, V. (2016), Imaging and image-based fluid transport modeling at the pore scale in geological materials: A practical introduction to the current state-of-the-art, Earth-Science Reviews, 155, 93-128, doi:10.1016/j.earscirev.2016.02.001.

Burdine, N. T. (1953), Relative permeability calculations from pore size distribution data. Society of Petroleum Engineers. doi:10.2118/225-G.

Cross, M. M. (1965), Rheology of non-Newtonian fluids: A new flow equation for pseudoplastic systems, Journal of Colloid Science, 20 (5), 417-437, doi:10.1016/0095-8522(65)90022-X.

Culligan, K.A., Wildenschild, D., Christensen, B.S.B., Gray, W., & Rivers, M.L. (2006), Pore-scale characteristics of multiphase flow in porous media: a comparison of air–water and oil–water experiments, Advances in Water Resources, 29, 227–238, doi:10.1016/j.advwatres.2005.03.021.

Dollimore, D. & Heal, G. R. (1964), An improved method for the calculation of pore size distribution from adsorption data, Journal of Applied Chemistry, 14, 109-114, doi:10.1002/jctb.5010140302

Doube, M., Kłosowski, M. M., Arganda-Carreras, I., Cordelières, F. P., Dougherty, R. P., Jackson, J. S., Schmid, B., Hutchinson, J. R., & Shefelbine, S. J. (2010), BoneJ: Free and extensible bone image analysis in ImageJ. Bone, 47 (6), 1076-1079, doi:10.1016/j.bone.2010.08.023.

Doyen, P. M. (1988), Permeability, conductivity, and pore geometry of sandstone, Journal of Geophysical Research: Solid Earth, 93 (B7), 7729-7740, doi:10.1029/JB093iB07p07729.

Gallegos, D. P. & Smith, D. M. (1988), A NMR technique for the analysis of pore structure: Determination of continuous pore size distributions, Journal of Colloid and Interface Science, 122(1), 143-153, doi:10.1016/0021-9797(88)90297-4.

Gao, Z. & Hu, Q. (2013), Estimating permeability using median pore-throat radius obtained from mercury intrusion porosimetry, Journal of Geophysics and Engineering, 10(2), 025014, doi:10.1088/1742-2132/10/2/025014.

Gerke, H. H., & M. T. van Genuchten (1993), A dual-porosity model for simulating the preferential movement of water and solutes in structured porous media, Water Resources Research, 29(2), 305–319, doi:10.1029/92WR02339.

Giesche, H. (2006), Mercury Porosimetry: A General (Practical) Overview. Particle & Particle Systems Characterization., 23: 9-19. doi:10.1002/ppsc.200601009.

Gostick, J. (2017), PoreSpy: Image analysis tools for tomograms of porous media. https://porespy.org.

Groena, J.C.,Peffera, L. A. A., & Pérez-Ramírez, J. (2003), Pore size determination in modified micro- and mesoporous materials. Pitfalls and limitations in gas adsorption data analysis, Microporous and Mesoporous Materials, 60(1-3), 1-17, doi:10.1016/S1387-1811(03)00339-1.

Hauswirth, S. C., Birak, P. S., & Miller, C. T. (2012), Mobilization of manufactured gas plant tar with alkaline flushing solutions, Environmental Science and Technology, 46 (1), 426-433, doi:10.1021/es202278s.

Hauswirth, S. C., & Miller, C. T. (2014), A comparison of physicochemical methods for the remediation of porous medium systems contaminated with tar, Journal of Contaminant Hydrology, 167, 44-60, doi:10.1016/j.jconhyd.2014.08.002.

Holzer, L., Stenzel, O., Pecho, O., Ott, T., Boiger, G., Gorbar, M., de Hazan, Y., Penner, D., Schneider, I., Cervera, R., & Gasser, P. (2016), Fundamental relationships between 3D pore topology, electrolyte conduction and flow properties: Towards knowledge-based design of ceramic diaphragms for sensor applications, Materials & Design, 99, 314-327, doi:10.1016/j.matdes.2016.03.034.

Jang, H. Y., Zhang, K., Chon, B. H., & Choi, H. J. (2015), Enhanced oil recovery performance and viscosity characteristics of polysaccharide xanthan gum solution, Journal of Industrial and Engineering Chemistry, 21, 741-745, doi:10.1016/j.jiec.2014.04.005.

Jerauld, G. R. & Salter, S. J. (1990), The effect of pore-structure on hysteresis in relative permeability and capillary pressure: Pore-level modeling, Transport in Porous Media, 5, 103-151, doi:10.1007/BF00144600.

Joekar-Niasar, V., Hassanizadeh, S.M. & Leijnse, A. (2008), Insights into the relationships among capillary pressure, saturation, interfacial area and relative permeability using pore-network modeling, Transport in Porous Media 74: 201, doi:10.1007/s11242-007-9191-7.

Kenyon, W. E., Howard, J. J., Sezginer, A., Straley, C., Matteson, A., Horkowitz, K., & Ehrlich, R. (1989), Pore-size distribution and NMR in microporous cherty sandstones, Society of Petrophysicists and Well-Log Analysts, SPWLA 30th Annual Logging Symposium, 11-14 June, Denver, Colorado.

Komlosh, M. E., Özarslan, E., Lizak, M. J., Horkay, F., & Schram, V., Shemesh, N., Cohen, Y., Basser, P. J. (2011), Pore diameter mapping using double pulsed-field gradient MRI and its validation using a novel glass capillary array phantom,Journal of Magnetic Resonance, 208(1), 128-135, doi:10.1016/j.jmr.2010.10.014.

Lakhtychkin, A., Eskin, D., & Vinogradov, O. (2012), Modelling of transport of two proppant-laden immiscible power-law fluids through an expanding fracture, The Canadian Journal of Chemical Engineering, 90 (3), 528-543, doi:10.1002/cjce.20694.

Larsbo, M., Roulier, S., Stenemo, F., Kasteel, R. & Jarvis, N. (2005) An Improved Dual-Permeability Model of Water Flow and Solute Transport in the Vadose Zone, Vadose Zone Journal, 4, 398–406, doi:10.2136/vzj2004.0137

Lindquist, W. B., A. Venkatarangan, J. Dunsmuir, and T. Wong (2000), Pore and throat size distributions measured from synchrotron X-ray tomographic images of Fontainebleau sandstones, Journal of Geophysical Reserach, 105(B9), 21509-21527, doi:10.1029/2000JB900208.

Loucks, R. G., Reed, R. M., Ruppel, S. C., & Jarvie, D.M. (2009), Morphology, Genesis, and Distribution of Nanometer-Scale Pores in Siliceous Mudstones of the Mississippian Barnett Shale. Journal of Sedimentary Research, 79(12), 848–861, doi:10.2110/jsr.2009.092.

Münch, B., & Holzer, L. (2008), Contradicting Geometrical Concepts in Pore Size Analysis Attained with Electron Microscopy and Mercury Intrusion. Journal of the American Ceramic Society, 91(12), 4059-4067, doi: 10.1111/j.1551-2916.2008.02736.x.

Omote, K. & Ito, Y. (2003), Small angle x-ray scattering for measuring pore-size distributions in porous low-κ films, Applied Physics Letters, 82, 544, doi:10.1063/1.1539546.

Otsu, N. (1979), A threshold selection method from gray-level histograms, IEEE Transactions on Systems, Man and Cybernetics, 9(1), 62-66, doi: 10.1109/TSMC.1979.4310076.

Oukhlef, A., Champmartin, S. & Ambari, A. (2014). Yield stress fluid method to determine the pore size distribution of a porous medium system, Journal of Non-Newtonian Fluid Mechanics, 204, 87-93, doi:0.1016/j.jnnfm.2013.12.004.

Rodriguez de Castro, A., Omari, A., Ahmadi–Sénichault, A. & Bruneau, D. (2014) Toward a new method of porosimetry: Principles and experiments. Transport in Porous Media, 101, 349–364, doi:10.1007/s11242-013-0248-5.

Rodríguez de Castro, A., Omari, A., Ahmadi-Sénichault, A., Savin, S. & Madariaga, L. (2016) Characterizing porous media with the yield stress fluids porosimetry method, Transport in Porous Media, 114(1), 213-233, doi:10.1007/s11242-016-0734-7.

Schroth, M., Istok, J., Ahearn, S., & Selker, J. (1996), Characterization of Miller-similar silica sands for laboratory hydrologic studies, Soil Science Society of America Journal, 60(5), 1331-1339, doi:10.2136/sssaj1996.03615995006000050007x.

Silva, J. A. K., Crimi, M., Palaia, T., Ko, S., & Davenport, S. (2017), Field demonstration of polymer-amended in situ chemical oxidation (PA-ISCO), Journal of Contaminant Hydrology, 199, 36-49, doi:10.1016/j.jconhyd.2017.03.001.

Sochi, T. (2010), Flow of non-Newtonian fluids in porous media, Journal of Polymer Science: Part B: Polymer Physics, 48, 2437-2767, doi:10.1002/polb.22144.

Sochi, T. (2015), Analytical solutions for the flow of Carreau and Cross fluids in circular pipes and thin slits, Rheologica Acta, 54, 745-756, doi: 10.1007/s00397-015-0863-x.

Srisutthiyakorn, N., & Mavko, G. M. (2017), What is the role of tortuosity in the Kozeny-Carman equation? Interpretation, 5(1), SB57-SB67, doi:10.1190/INT-2016-0080.1.

Stewart, R. D., Najm, M. R. A., Rupp, D. E., & Selker, J. S. (2014), Nondestructive quantification of macropore volume using shear-thinning fluid. Soil Science Society of America Journal, 78(2), 445-453, doi:10.2136/sssaj2013.08.0346.

Strange, J. H., Rahman, M. & Smith, E. G. (1993) Characterization of porous solids by NMR, Physical Review Letters, 71(21), 3589, doi:10.1103/PhysRevLett.71.3589.

Tosco, T., & Sethi, R. (2010), Transport of non-Newtonian suspensions of highly concentrated micro- and nanoscale iron particles in porous media: A modeling approach. Environmental Science and Technology, 44(23), 9062-9068, doi:10.1021/es100868n.

Vogel, H. (1997), Morphological determination of pore connectivity as a function of pore size using serial sections. European Journal of Soil Science, *48*(3), 365-377, doi:10.1111/j.1365-2389.1997.tb00203.x.

Vogel, T., Gerke, H., Zhang, R., & Van Genuchten, M. (2000), Modeling flow and transport in a two-dimensional dual-permeability system with spatially variable hydraulic properties. Journal of Hydrology, *238*(1-2), 78-89, doi:10.1016/S0022-1694(00)00327-9.

Wildenschild, D. & Sheppard, A. P. (2013), X-ray imaging and analysis techniques for quantifying pore-scale structure and processes in subsurface porous medium systems, Advances in Water Resources, 51, 217-246, doi:10.1016/j.advwatres.2012.07.018.

Wise, W. R. (1992), A new insight on pore structure and permeability. Water Resources Research, 28(1), 189-198, doi:10.1029/91WR02522.

Xiong, Q., Baychev, T. G., & Jivkov, A. P. (2016), Review of pore network modelling of porous media: Experimental characterisations, network constructions and applications to reactive transport. Journal of Contaminant Hydrology, 192, 101-117, doi:10.1016/j.jconhyd.2016.07.002.

Zhou, S., Liu, D., Cai, Y., Yao, Y., Che, Y., Liu, Z. (2017), Multi-scale fractal characterizations of lignite, subbituminous and high-volatile bituminous coals pores by mercury intrusion porosimetry, Journal of Natural Gas Science and Engineering, 44, 338-350, doi:10.1016/j.jngse.2017.04.021.

Figure 1 - Summary of the µCT image processing method. Clockwise from upper left: initial cross-sectional image slice; cropping to remove glass column from image and create a square image; segmentation using the Otsu algorithm in ImageJ; pore size distribution determination (2D representation of BJT distance map shown). 20/30 Accusand shown.

Figure 2. Pore size distributions of the four sands from four µCT image processing methods: PSD = continuous pore size distribution of the *xlib* ImageJ plugin; MIP = mercury porosimetry simulation of the *xlib* ImageJ plugin; BJT = thickness function of BoneJ plugin for ImageJ; PSF = pore size function of Porespy code. Lines represent normal distributions fit to the data in Matlab.

Figure 3. Pore size distributions for Problem Type 3 with N=4. For each medium, 12 model runs were conducted with different sets of fluid/flow rate experimental data, with each run depicted with a distinct symbol. Solid and dashed lines represent normal distributions from the µCT data for the PSD and MIP methods, respectively. Pore radii are shown as normalized volume fractions, assuming both cylindrical (left figure of each pair) and spherical radii (right figures).

Figure 4. Box plots displaying the volume-averaged mean pore radii calculated from µCT data and modeling results assuming cylindrical pores (top) and spherical pores (bottom). The solid horizontal line represents mean radius from PSF and the dashed horizontal line represents the mean radius from MIP. PT1S = Problem Type 1 with varying fluids/flow rates (N=4); PT1R = Problem Type 1 with varied radii (N=4); PT2S = Problem Type 2 with varying fluid/flow rates; PT2W = Problem Type 2, varied weights; PT3 = Problem Type 3. Tortuosity = 2 for all runs. A summary of all runs performed is available in Table S2 of the SI.

Figure 5. Effect of Cross model parameters on the volume-weighted mean pore radius. The ANA model (Problem Type 1) was run for a set of experimental inputs for 20/30 Accusand (N=4), varying each parameter independently. Volume-weighted mean pore radii were calculated for each model run and reported as the variation from the case with the original parameters.

Figure 6. (a.) Simulated soil-water retention curves for 20/30 Accusand using results of Type 2 model runs with varying values of N (lines) shown with experimental results for the same sand extracted from Ref. 1. The N=1 data is based on the radius obtained when only water is used. For all values of N, the simulated results closely follow the experimental data, with deviations primarily occurring at lower saturations. (b.) The NRMSE shows a significant decrease at N=4 and continues to decrease through N=19. The dashed line represents the error for the drainage curve simulated with the MIP µCT pore size distribution (consisting of 34 radii).

Figure 1.

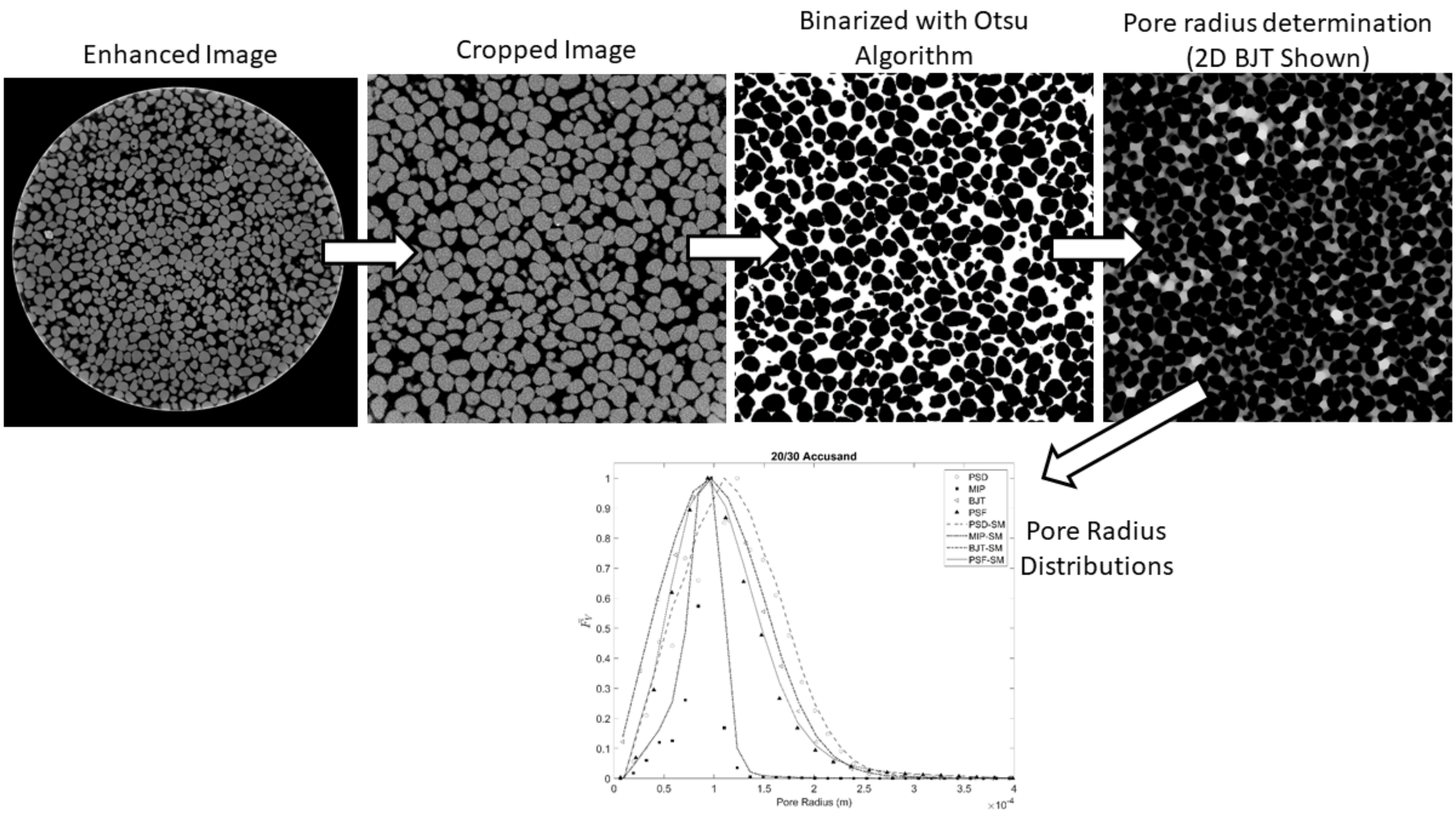
Enhanced Image
Cropped Image
Binarized with Otsu Algorithm
Pore radius determination (2D BJT Shown)
Pore Radius Distributions
20/30 Accusand
PSD
MIP
BJT
PSF
PSD-SM
MIP-SM
BJT-SM
PSF-SM
Pore Radius (m)
×10^-4

Figure 2.

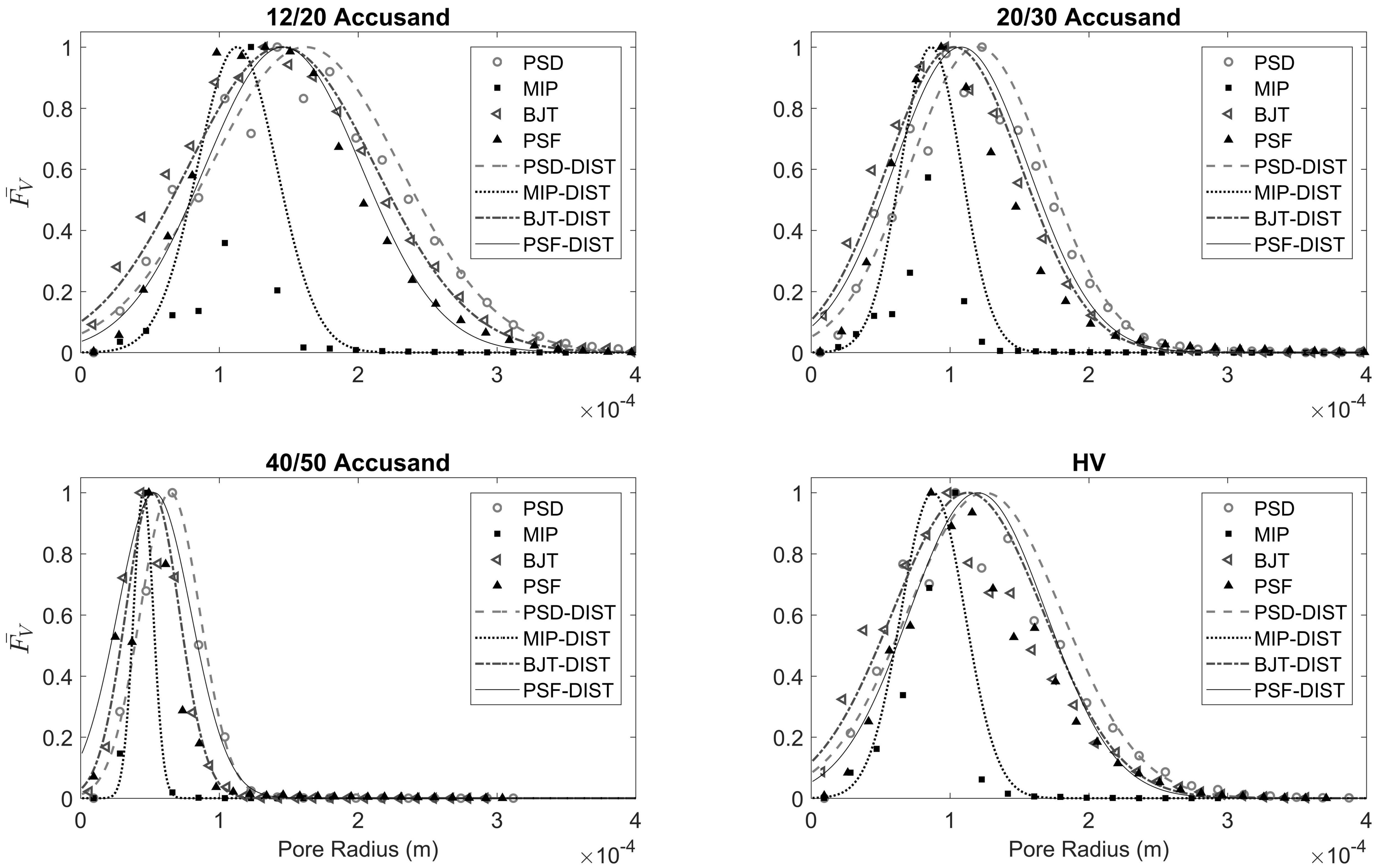
12/20 Accusand
20/30 Accusand
40/50 Accusand
HV
PSD
MIP
BJT
PSF
PSD-DIST
MIP-DIST
BJT-DIST
PSF-DIST
$\bar{F}_V$
Pore Radius (m)
$\times 10^{-4}$

Figure 3.

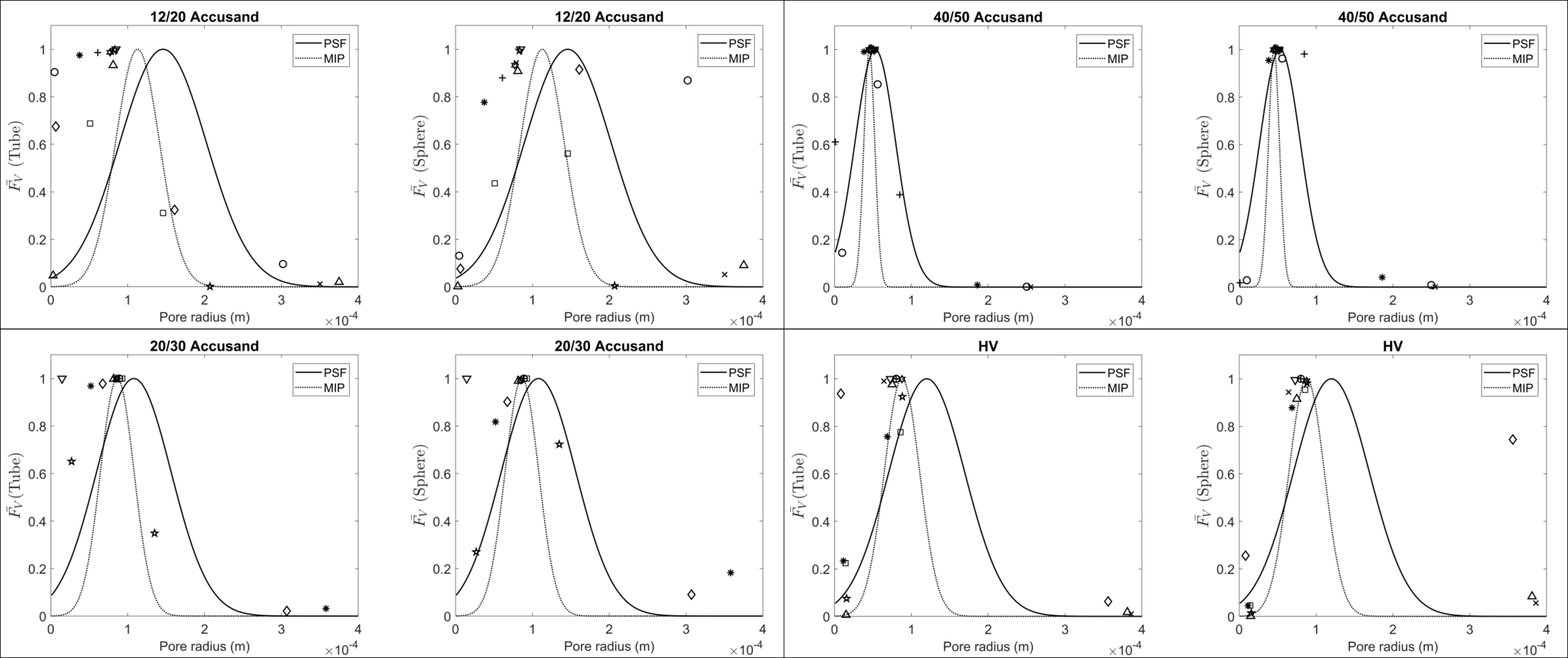
12/20 Accusand
12/20 Accusand
40/50 Accusand
40/50 Accusand
20/30 Accusand
20/30 Accusand
HV
HV
PSF
MIP
$\bar{F}_V$ (Tube)
$\bar{F}_V$ (Sphere)
Pore radius (m)
$\times 10^{-4}$
0
0.2
0.4
0.6
0.8
1
0
1
2
3
4

Figure 4.

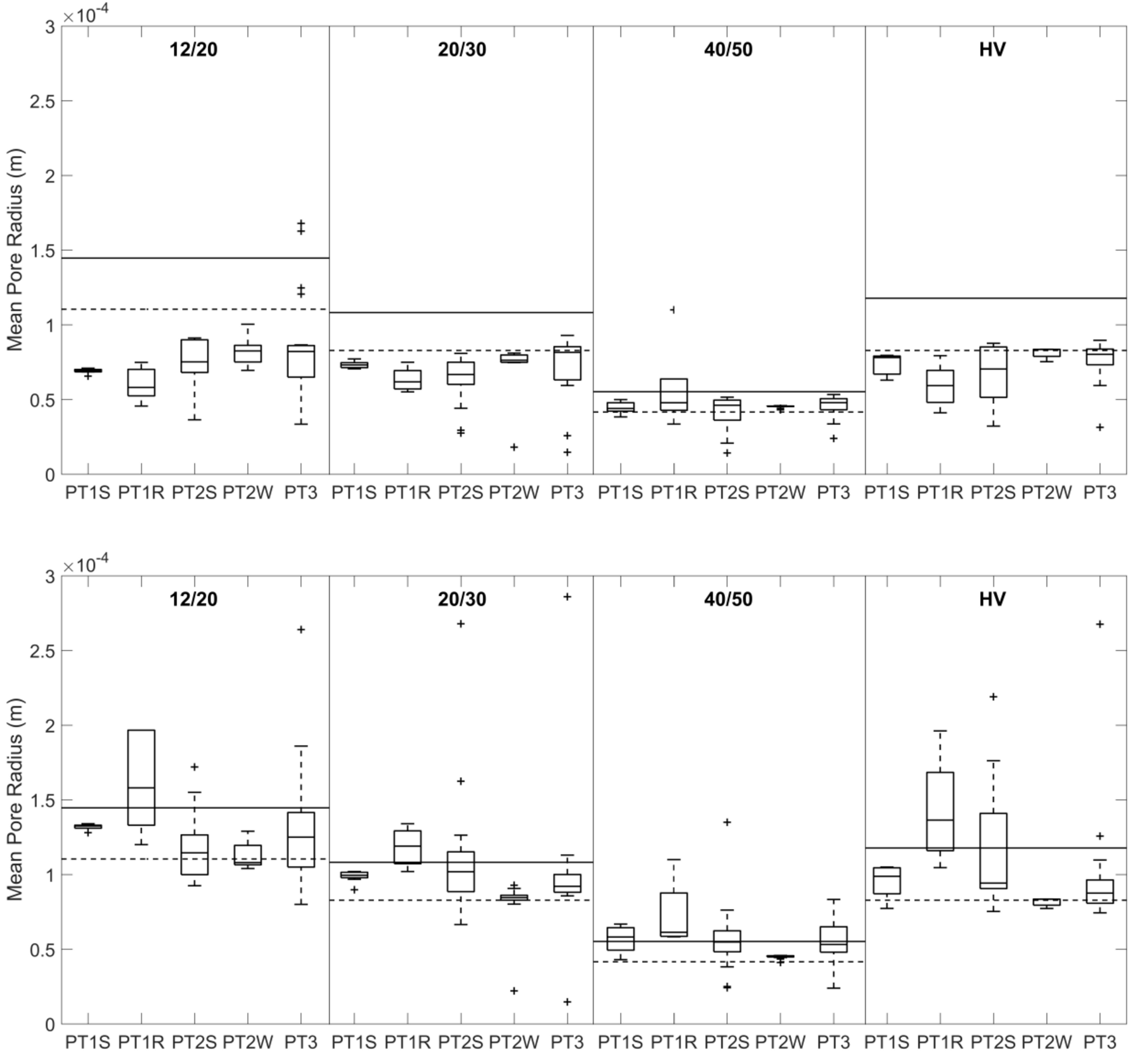
×10^-4
Mean Pore Radius (m)
12/20
20/30
40/50
HV
PT1S PT1R PT2S PT2W PT3
3
2.5
2
1.5
1
0.5
0

Figure 5.

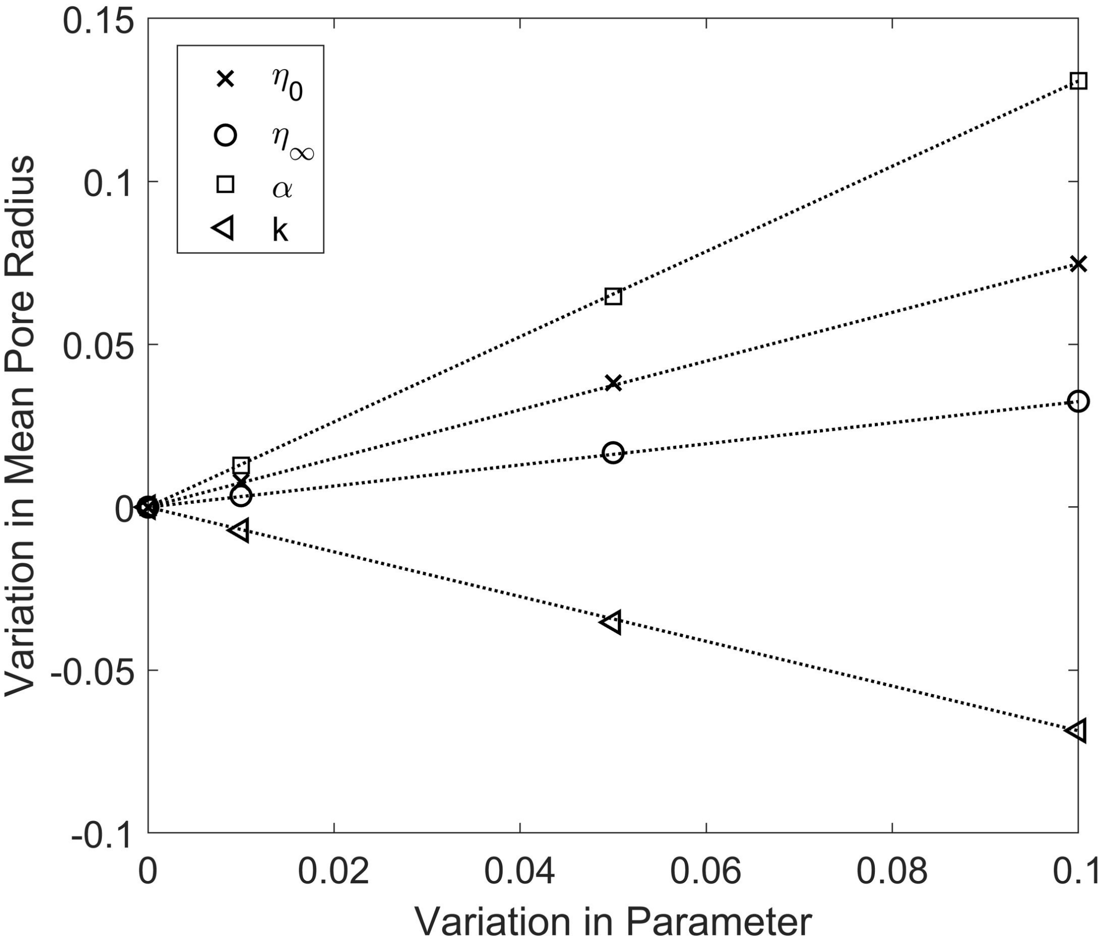

Variation in Mean Pore Radius
Variation in Parameter
η_0
η_∞
α
k
0.15
0.1
0.05
0
-0.05
-0.1
0
0.02
0.04
0.06
0.08
0.1

Figure 6.

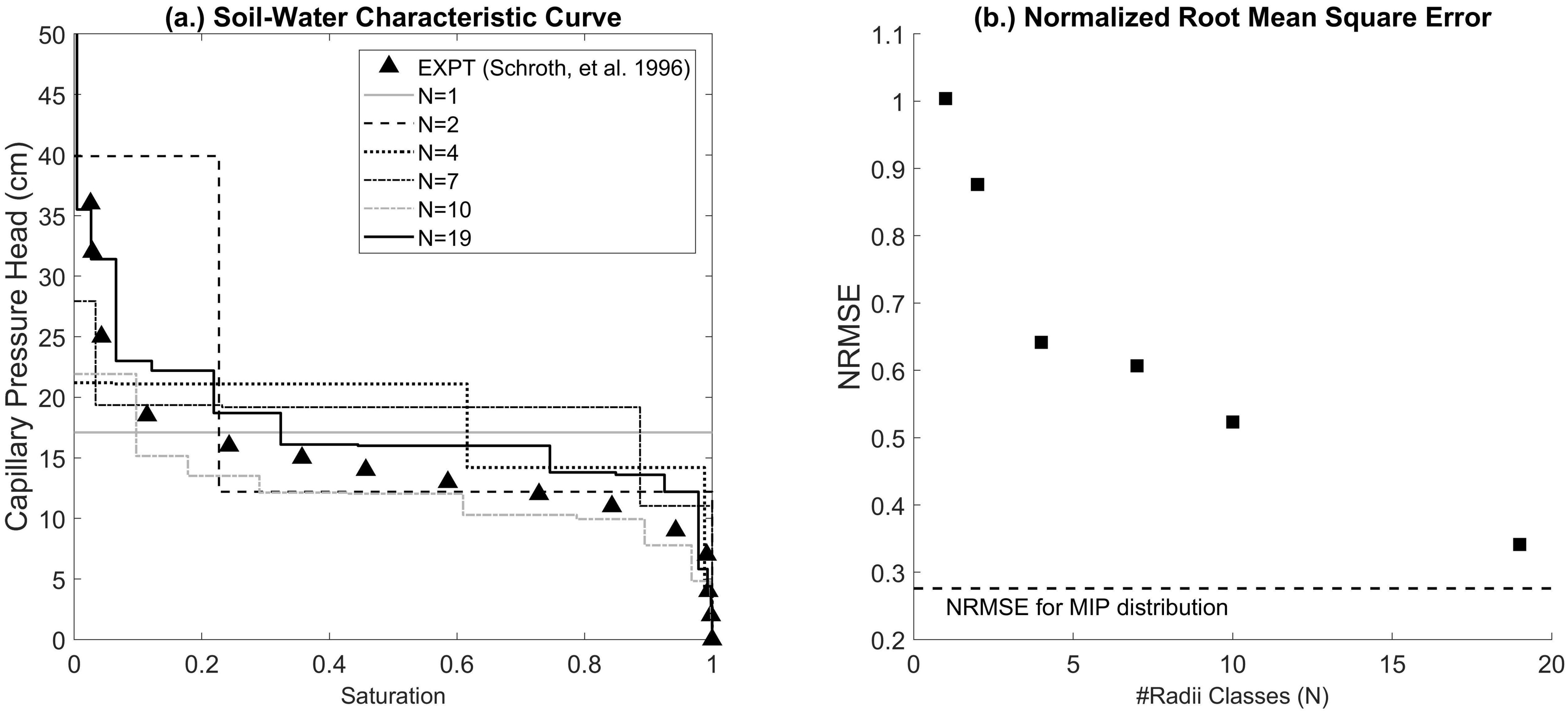
(a.) Soil-Water Characteristic Curve
Capillary Pressure Head (cm)
Saturation
EXPT (Schroth, et al. 1996)
N=1
N=2
N=4
N=7
N=10
N=19
0
5
10
15
20
25
30
35
40
45
50
0.2
0.4
0.6
0.8
1
(b.) Normalized Root Mean Square Error
NRMSE
#Radii Classes (N)
NRMSE for MIP distribution
0.2
0.3
0.4
0.5
0.6
0.7
0.8
0.9
1
1.1
0
5
10
15
20